would have to dissociate from the DNA binding domain. Second, a processive 360° rotation, or multiples thereof, has been observed when using an artificial substrate that has two sites mismatching in the central region of site I (*27*) and is not easily explained by the domain swap model.

The synaptosome. How this synaptic tetramer bound to site I can be accommodated in a model of the complete synaptosome is unclear. The relationship between the synaptic tetramer seen here and the rest of the complex must differ from the model proposed earlier (*14*) for a synaptosome structure. That model was constructed making the assumption, on the basis of extensive genetic data (*12*, *13*), that dimers bound to sites I, II, and III of the same *res* site DNA are making the 2, 3′ interactions. There are, however, no biochemical or structural data to support the proposed interaction between the three resolvase dimers bound to each of the two *res* sites. Our attempts to model the synaptic complex at site I (via the R and R′ subunits) onto the structure of a site II and III complex presumed in earlier models (*10*, *14*) show that, although the dimensions roughly match, an interaction of the 2, 3′ type cannot be made.

We presume that resolvase dimers bound to sites II and III of two *res* sites contained in negatively supercoiled DNA are able to synapse and present two dimers bound to site I DNAs in such a manner that they promote the formation of the synaptic complex structure seen here. Perhaps two resolvase dimers are bound to the two site I DNAs in a presynaptic conformation initially and then form a synaptic tetramer at site I, facilitated by an increase in the local concentration and orientation of site I dimers by the rest of the synaptosome. However, the transition to the tetramer structure by the site I–bound resolvase subunits is likely accompanied by release of their 2,3′ interactions with the rest of the complex. It will doubtless be necessary to determine the structure of the whole synaptosome in order to understand how resolvase dimers bound to sites II and III promote synapsis at site I.

References and Notes

1. N. Craig, R. Craigie, M. Gellert, A. Lambowitz, Eds., *Mobile DNA II* [American Society for Microbiology (ASM), Washington, DC, 2002].
2. N. D. F. Grindley, in (*1*), p. 272.
3. R. R. Reed, N. D. F. Grindley, *Cell* **25**, 721 (1981).
4. G. F. Hatfull, N. D. F. Grindley, *Proc. Natl. Acad. Sci. U.S.A.* **83**, 5429 (1986).
5. S. A. Wasserman, J. M. Dungan, N. R. Cozzarelli, *Science* **229**, 171 (1985).
6. W. M. Stark, D. J. Sherratt, M. R. Boocock, *Cell* **58**, 779 (1989).
7. W. M. Stark, M. R. Boocock, *J. Mol. Biol.* **239**, 25 (1994).
8. M. R. Sanderson *et al.*, *Cell* **63**, 1323 (1990).
9. P. A. Rice, T. A. Steitz, *Structure* **2**, 371 (1994).
10. P. A. Rice, T. A. Steitz, *EMBO J.* **13**, 1514 (1994).
11. W. Yang, T. A. Steitz, *Cell* **82**, 193 (1995).
12. R. E. Hughes, G. F. Hatfull, P. Rice, T. A. Steitz, N. D. F. Grindley, *Cell* **63**, 1331 (1990).
13. L. L. Murley, N. D. F. Grindley, *Cell* **95**, 553 (1998).
14. G. J. Sarkis *et al.*, *Mol. Cell* **8**, 623 (2001).
15. F. Guo, D. N. Gopaul, G. D. van Duyne, *Nature* **389**, 40 (1997).
16. A. E. Leschziner, N. D. F. Grindley, *Mol. Cell* **12**, 775 (2003).
17. M. Nollmann, J. He, O. Byron, W. M. Stark, *Mol Cell.* **16**, 127 (2004).
18. P. H. Arnold, D. G. Blake, N. D. F. Grindley, M. R. Boocock, W. M. Stark, *EMBO J.* **18**, 1407 (1999).
19. Protein Data Bank codes are 1ZR2 and 1ZR4.
20. Materials and methods are available as supporting materials on *Science* Online.
21. Single-letter abbreviations for the amino acid residues are as follows: A, Ala; C, Cys; D, Asp; E, Glu; G, Gly; K, Lys; L, Leu; Q, Gln; R, Arg; S, Ser; V, Val; and Y, Tyr.
22. W. G. Krebs, M. Gerstein, *Nucleic Acids Res.* **28**, 1665 (2000).
23. Y. Chen, P. A. Rice, *Annu. Rev. Biophys. Biomol. Struct.* **32**, 135 (2003).
24. A. T. Brünger *et al.*, *Acta Crystallogr.* **D54**, 905 (1998).
25. G. Dhar, E. R. Sanders, R. C. Johnson, *Cell* **119**, 33 (2004).
26. C. Chothia, J. Janin, *Nature* **256**, 705 (1975).
27. M. J. McIlwraith, M. R. Boocock, W. M. Stark, *J. Mol. Biol.* **266**, 108 (1997).

28. This research was supported by NIH grants GM28470 to N.D.F.G. and GM57510 to T.A.S. The structures and the structure factors have been deposited in the Protein Data Bank under codes 1ZR2 and 1ZR4.

Supporting Online Material
www.sciencemag.org/cgi/content/full/1112064/DC1
SOM Text
Figs. S1 to S4
References and Notes
Movies S1 to S4

9 March 2005; accepted 15 June 2005
Published online 30 June 2005;
10.1126/science.1112064
Include this information when citing this paper.

REPORTS

Strong, Transparent, Multifunctional, Carbon Nanotube Sheets

Mei Zhang,[1] Shaoli Fang,[1] Anvar A. Zakhidov,[1] Sergey B. Lee,[1] Ali E. Aliev,[1] Christopher D. Williams,[1] Ken R. Atkinson,[2] Ray H. Baughman[1]*

Individual carbon nanotubes are like minute bits of string, and many trillions of these invisible strings must be assembled to make useful macroscopic articles. We demonstrated such assembly at rates above 7 meters per minute by cooperatively rotating carbon nanotubes in vertically oriented nanotube arrays (forests) and made 5-centimeter-wide, meter-long transparent sheets. These self-supporting nanotube sheets are initially formed as a highly anisotropic electronically conducting aerogel that can be densified into strong sheets that are as thin as 50 nanometers. The measured gravimetric strength of orthogonally oriented sheet arrays exceeds that of sheets of high-strength steel. These nanotube sheets have been used in laboratory demonstrations for the microwave bonding of plastics and for making transparent, highly elastomeric electrodes; planar sources of polarized broad-band radiation; conducting appliqués; and flexible organic light-emitting diodes.

Carbon nanotube sheets are usually made using techniques from the ancient art of papermaking, typically by a week-long filtration of nanotubes dispersed in water and then peeling the dried nanotubes as a layer from the filter (*1*, *2*). Variations of the filtration route produce ultrathin nanotube sheets that are highly transparent and highly conducting (*3*, *4*). Although filtration-produced sheets are normally isotropic within the sheet plane, sheets having partial nanotube alignment result from the application of high magnetic fields during filtration (*5*) and from mechanical rubbing of nanotubes that are vertically trapped in filter pores (*6*). In other important advances, nanotube sheets have been fabricated from a nanotube aerogel (*7*), by Langmuir-Blodgett deposition (*8*), by casting from oleum (*9*), and by spin coating (*10*).

We produced highly oriented, free-standing nanotube sheets by a solid-state process that appears to be scalable for continuous high-rate production. This development builds on previous advances in the dry-state spinning of nanotube yarns from forests (*11*) and the introduction of twist to increase sheet strength a thousandfold (*12*).

[1]NanoTech Institute, University of Texas at Dallas, Richardson, TX 75083–0688, USA. [2]Commonwealth Scientific and Industrial Research Organization Textile & Fibre Technology, Post Office Box 21, Belmont, Victoria 3216, Australia.

*To whom correspondence should be addressed. E-mail: ray.baughman@utdallas.edu

These transparent nanotube sheets were drawn from a sidewall of multiwalled nanotube (MWNT) forests that were synthesized by catalytic chemical vapor deposition, using acetylene gas as the carbon source (*12*). The MWNTs were ~10 nm in diameter, and the range of investigated forest heights was 70 to 300 μm. Draw was initiated using an adhesive strip, like that on a 3M Post-it Note, to contact MWNTs teased from the forest sidewall. Meter-long sheets, up to 5 cm wide, were then made at 1 m/min by hand drawing (Fig. 1A and movie S1). Despite a measured areal density of only ~2.7 μg/cm^2, these 500-cm^2 sheets were self-supporting during draw. A 1-cm length of 245-μm-high forest converts to about a 3-m-long freestanding MWNT sheet. The sheet production rate was increased to 5 m/min by using an automated linear translation stage to accomplish draw (Fig. 1B) and was increased to up to 10 m/min by winding the sheet on a rotating centimeter-diameter plastic cylinder. The sheet fabrication process is quite robust, and no fundamental limitations on sheet width and length are apparent: The obtained 5-cm sheet width equaled the forest width when the draw rate was about 5 m/min or lower. At constant draw rates above ~7 m/min, the sheets progressively narrowed, and MWNT fibrils began to break at the intersection between the sheet sides and the forest.

This draw process does not work for all MWNT forests, and the maximum allowable draw rate depends on the structure of the forest. Intermittent bundling within the forest seems to be important, in which individual nanotubes migrate from one bundle of a few nanotubes to another. Bundled nanotubes are simultaneously pulled from different elevations in the forest sidewall, so that they join with bundled nanotubes that have reached the top and bottom of the forest, thereby minimizing breaks in the resulting fibrils (Fig. 1, B and C). Disordered regions exist at the top and bottom of the forests, where a fraction of the nanotubes form loops, which might help maintain continuity. For forests having similar topology, the highest forests were easiest to draw into sheets, probably because increasing the nanotube length increases interfibril mechanical coupling within the sheets.

Nanotube orientation is evident in the micrograph of Fig. 1B and in ultraviolet (UV)–visible absorption and Raman scattering measurements for as-drawn single MWNT sheets and sheet stacks. Depending on the sample, the ratio of Raman intensity (632.8-nm excitation) of the G band for polarization parallel and perpendicular to the draw direction is between 5.5 and 7.0 for the VV configuration (parallel polarization for incident light and Raman signal), which corresponds to polarization degrees of 0.69 and 0.75, respectively, for the investigated four-sheet stacks (fig. S1). Ignoring the effect of light scattering, the ratio of absorption coefficients for parallel and perpendicular polarizations for the as-drawn single sheet was 4.1 at 633 nm and monotonically increased to 6.0 at 2.2 μm.

The thickness of the as-produced MWNT sheet increased with increasing forest height and was ~18 μm in scanning electron microscopy (SEM) images of a sheet drawn from a 245-μm-high forest. From this thickness and the measured areal sheet density of ~2.7 μg/cm^2, the volumetric density was 0.0015 g/cm^3. Hence, the as-produced sheets are an electronically conducting, highly anisotropic aerogel. These sheets, which can easily be stacked (Fig. 1D), can support millimeter-sized liquid droplets that are 50,000 times more massive than the supporting sheet region in contact with the droplet (Fig. 1E).

We can easily densify these highly anisotropic aerogel sheets into highly oriented sheets having a thickness of 50 nm (*13*) and a density of ~0.5 g/cm^3. We obtain this 360-fold density increase simply by causing the as-produced sheet to adhere to a planar substrate (such as glass, many plastics, silicon, gold, copper, aluminum, or steel) by contact, vertically immersing the substrate with the attached MWNT sheet in a liquid (such as ethanol) along the nanotube alignment direction, and then retracting the substrate from the liquid. Surface tension effects during ethanol evaporation shrink the aerogel sheet thickness to ~50 nm. SEM micrographs taken normal to the sheet plane suggest a decrease in nanotube orientation as a result of densification. This observation is deceptive: The collapse of ~20-μm sheets to ~50-nm sheets without changes in lateral sheet dimensions means that out-of-plane deviations in nanotube orientation become in-plane deviations that are noticeable in the SEM micrographs. The aerogel sheets can be effectively glued to a substrate by contacting selected regions with ethanol and allowing evaporation to densify the aerogel sheet. Adhesion increases because the collapse of aerogel thickness increases the contact area between the nanotubes and the substrate.

The sheet resistance in the draw direction changes by <10% upon sheet densification by a factor of ~360, which increases sheet transparency (Fig. 2, A and B). Although the

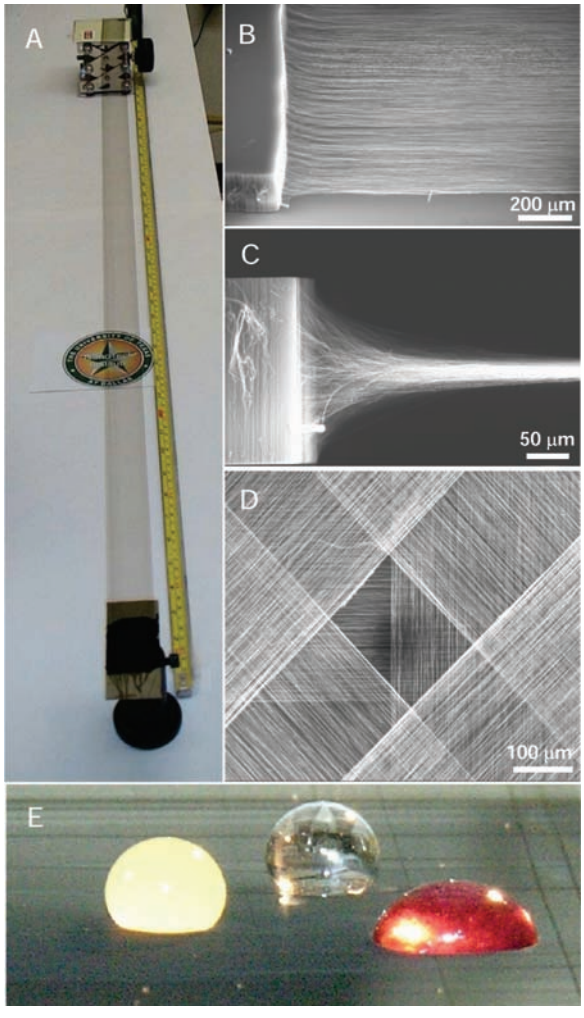

Fig. 1. MWNT forest conversion into sheets and assemblies of those sheets. (**A**) Photograph of a self-supporting 3.4-cm-wide, meter-long MWNT sheet that has been hand drawn from a nanotube forest at an average rate of 1 m/min. Its transparency is illustrated by the visibility of the NanoTech Institute logo that is behind the MWNT sheet. (**B**) SEM image, at a 35° angle with respect to the forest plane, capturing a MWNT forest being drawn into a sheet. (**C**) SEM micrograph showing the cooperative 90° rotation of MWNTs in a forest to form a sheet. (**D**) SEM micrograph of a two-dimensionally re-reinforced structure fabricated by overlaying four nanotube sheets with a 45° shift in orientation between successive sheets. The dark circle is the shadow of the in-lens detector. (**E**) Photograph showing two orthogonal as-drawn nanotube sheets supporting droplets of water (~2.5 mm in diameter), orange juice, and grape juice, where the mass of the droplet is up to 50,000 times that of the contacting nanotube sheets. The aerogel sheet regions under the aqueous droplets are densified during water evaporation.

anisotropy ratio for sheet resistance decreases from 50 to 70 for the undensified sheets to 10 to 20 for the densified sheets, this anisotropy ratio for the densified sheets is nearly temperature-invariant. In fact, the temperature dependence of sheet resistivity is nearly the same for the forest-drawn densified nanotube sheets and for sheets made by the filtration route using the same forest-grown MWNTs, and is much smaller than for single-walled nanotube (SWNT) sheets fabricated by filtration (*14*) (Fig. 2A). In addition, the low-frequency (f) noise power density in the draw direction for a densified forest-drawn sheet is 10^4 and is 10 times lower than for ordinary filtration-produced sheets of SWNTs and MWNTs, respectively (Fig. 2C). The literature reports high $1/f$ noise for individual SWNTs and SWNT mats (*15*) and low noise having either a $1/f$ (*16*) or a $1/f^2$ dependence (*17*) for individual MWNTs. In contrast with the latter single-MWNT results, the noise power density for our densified MWNT sheets has a $1/f$ frequency dependence.

A possible explanation for these electronic properties is found in SEM micrographs (fig. S2), which indicate that up to ~50-nm-wide fibrils (containing many bundled MWNTs) laterally fork and then eventually recombine with the forked legs of other fibrils to form a laterally extended network. High resistance of interfibril contacts formed during densification, as compared with those within the original fibril network, might explain why sheet resistance changes little as a result of over 300-fold sheet densification. Because low-frequency noise inversely depends on the number of atoms at resistive contacts (*15*), the low $1/f$ noise of the solid-state fabricated MWNT sheets could result from the long path length where MWNTs overlap within the fibril network. Whatever the explanation for these properties, the low electrical noise and low temperature coefficient of resistivity for the forest-drawn sheets could be important for electronic applications such as chemical sensors.

The densified nanotube sheets showed high transparency in combination with usable electrical conductivity, a combination needed for such applications as displays, video recorders, solar cells, and solid-state lighting (*3*). The sheet resistivity was ~700 ohms per square in the draw direction before and after densification for the forest-drawn sheets, and 10 to 20 times higher in the orthogonal in-plane direction for the densified sheet. The transmittance for the densified MWNT sheet was >85% for perpendicular polarization, >65% for parallel polarization between 400 nm and 2 μm, and >85% for unpolarized radiation between 1.5 and 10 μm (Fig. 2B). These MWNT sheets will adhere to transparencies made of poly(ethylene terephthalate) and to silicone rubber sheets, thereby providing transparent bilayer composites that can be bent in any direction without causing a substantial decrease in electrical conductivity (movie S2). This ability to bend without degradation of electronic conductivity is important for flexible electronic circuits and is not found in conventional transparent conductors such as indium tin oxide (ITO).

After an initial conditioning strain cycle, in which conductivity decreased ~6% with increasing strain, the nanotube/elastomer sheet was repeatably deformable over 100% strain (fig. S3) without causing a substantial change in conductance (*18*). Ordinary conductors cannot undergo nearly such large strains without losing electrical contact with the actuating material. Although conducting greases are used to maintain electrical contact to electrostrictive actuator materials that generate 100% or higher strains (*19*), these greases are not suitable for use as electrodes for stacks of electrostrictive sheets that can generate large forces and high strains without requiring several-thousand-volt applied potentials.

Although no alternative solid-state conductors combine elastic deformability to 100% strain and essentially constant electronic conductivity, transparent doped SWNT sheets having ~20 times higher electrical conductivity are known (*3*). The transparency of those SWNT sheets (either doped or undoped) strongly depends on wavelength in the visible and near-infrared. Thus, the monotonic increase in transmittance with increasing wavelength (Fig. 2B) of our MWNT sheets provides an advantage for broadband applications. Also, the electrical conductivity of those SWNT sheets decreases 10 times upon dedoping. Extension of the present solid-state sheet fabrication technology to doped MWNTs and doped SWNTs is desirable in order to increase electrical conductivity for transparent conductor applications, and even the latter appears feasible because of the recent development of 2.5-mm-high nanotube forests comprising SWNTs (*20*).

The forest-drawn MWNT sheets can be conveniently assembled into biaxially reinforced sheet arrays (Fig. 1D) and as conducting layers on nonplanar surfaces, such as by helically wrapping a sheet strip on a millimeter- or larger-diameter cylinder (fig. S4). Chiral structures, which will likely be optically active for long infrared and microwave wavelengths, can be made by stacking parallel sheets so that the orientation direction varies helically along the stack thickness and then densifying the stacked array so that the individual sheet thickness is ~50 nm.

Especially considering the absence of polymer binder, the mechanical properties of the

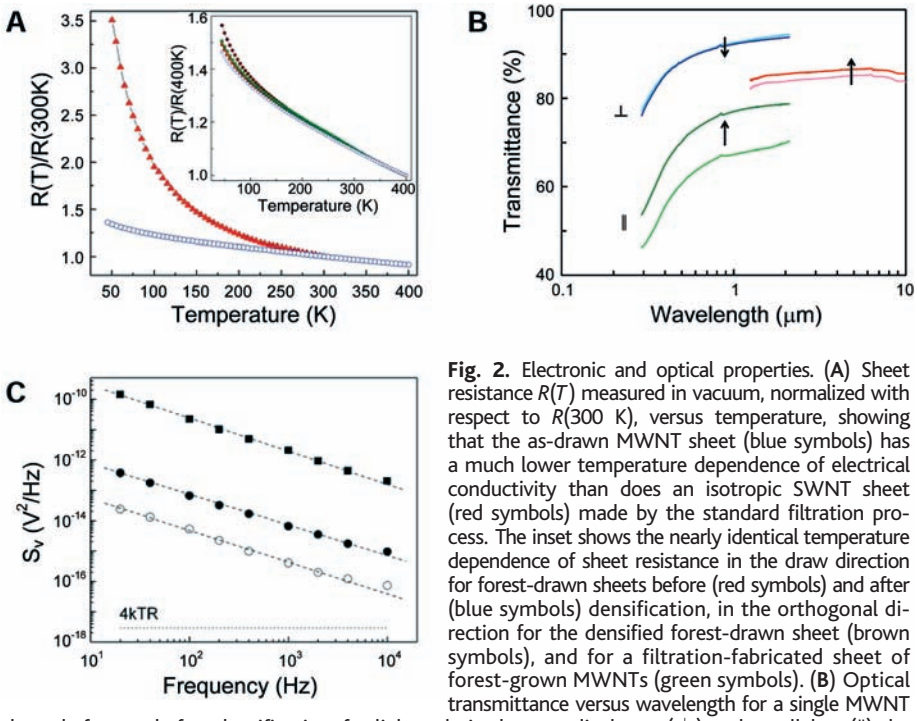

Fig. 2. Electronic and optical properties. (**A**) Sheet resistance $R(T)$ measured in vacuum, normalized with respect to R(300 K), versus temperature, showing that the as-drawn MWNT sheet (blue symbols) has a much lower temperature dependence of electrical conductivity than does an isotropic SWNT sheet (red symbols) made by the standard filtration process. The inset shows the nearly identical temperature dependence of sheet resistance in the draw direction for forest-drawn sheets before (red symbols) and after (blue symbols) densification, in the orthogonal direction for the densified forest-drawn sheet (brown symbols), and for a filtration-fabricated sheet of forest-grown MWNTs (green symbols). (**B**) Optical transmittance versus wavelength for a single MWNT sheet, before and after densification, for light polarized perpendicular to (⊥) and parallel to (∥) the draw direction and for unpolarized light (the two curves on the right), where the arrow points from the data for the undensified sample to those for the densified sample. (**C**) Noise power density (S_V, measured in air for 10-mA biasing) versus frequency (f) for a densified forest-drawn MWNT sheet (open circles), compared with that for ordinary filtration-produced MWNT sheets (solid circles) and SWNT sheets (solid rectangles) having the same 40-ohm resistance. The dashed lines are data fits for a $1/f^{\alpha}$ dependence, where α is 0.98 ± 0.04, 0.97 ± 0.02, and 1.20 ± 0.02 for the lower, middle, and upper data sets, respectively. The lower-limit noise power at temperature T (the product of 4 kT and the sample resistance R, where k is Boltzmann's constant) is indicated by the horizontal dotted line.

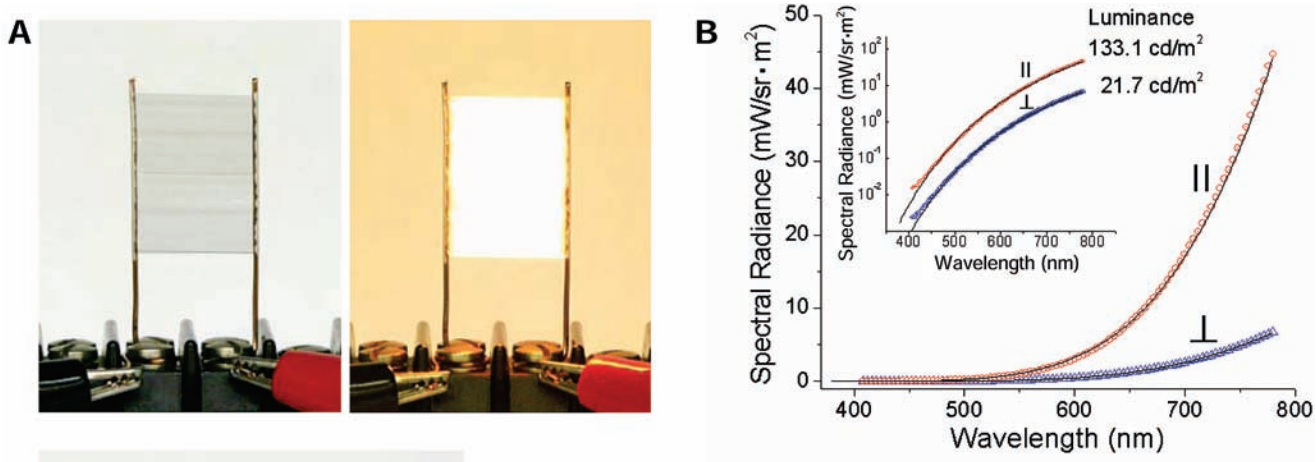

Fig. 3. Application as a broadband source of polarized incandescent light and for the microwave welding of plastics. (**A**) Photograph showing a free-standing undensified MWNT sheet (16 mm by 22 mm) used as a planar incandescent light source that emits polarized radiation. The background color of the unheated sheet (left) and the incandescent sheet (right) differs because of reflected incandescent light from a white paper sheet that is behind the light source. (**B**) Spectral radiance in directions parallel to (∥) and perpendicular to (⊥) the draw direction of an as-drawn undensified MWNT sheet after an added inelastic stretch in the initial draw direction of 2.5%. The luminance polarized parallel to the sheet draw direction for the indicated spectral range is 6.1 times higher than for the perpendicularly polarized luminance, which corresponds to a polarization factor of 0.72. The inset shows these data on a semilogarithmic scale. Underlying solid lines (largely obscured by coincidence with the data points) are data fits assuming black-body radiation with T = 1410 K. (**C**) Photograph of two 5-mm-thick Plexiglas plates that have been welded together by microwave-induced heating of an as-drawn MWNT sheet strip that was sandwiched between these plates. The nanotube sheet strip at the welded interface (see arrow for vertical extension) remains oriented, highly conducting, and transparent, as indicated by the visibility of "UTD" printed on an underlying paper sheet.

aerogel-like and densified MWNT sheets are unexpectedly high, which is probably a consequence of the interconnected fibril network (fig. S2). The density-normalized mechanical strength is much more accurately determined than mechanical strength, because the sheet thickness is less reliably measured than the ratio of maximum force to mass-per-length in the stretch direction. Stacks of undensified sheets have an observed tensile strength of between 120 and 144 MPa/(g/cm^3) (fig. S5, A and B). A densified stack containing 18 identically oriented sheets had a strength of 465 MPa/(g/cm^3), which decreased to 175 MPa/(g/cm^3) when neighboring sheets in the stack were orthogonally oriented to make a densified biaxial structure. These density-normalized strengths are already comparable to or greater than the ~160 MPa/(g/cm^3) strength of the Mylar and Kapton films used for ultralight air vehicles and proposed for use in solar sails for space applications (*21*) and those for ultra–high-strength steel [~125 MPa/(g/cm^3)] and aluminum alloy [~250 MPa/(g/cm^3)] sheets.

Sheets generally have much lower limiting strengths than do fibers of the same material. However, at a value of 465 MPa/(g/cm^3), the tensile strength of the densified MWNT sheet is comparable to or exceeds reported values for nanotube fibers and yarns that do not include a binding agent: 575 MPa/(g/cm^3) for forest-spun twisted MWNT yarns (*12*), 500 MPa/(g/cm^3) for aerogel-spun yarns (*7*), 105 MPa/(g/cm^3) for SWNT yarns spun from superacids (*22*), and 65 MPa/(g/cm^3) for SWNT yarns spun using an acidic coagulation bath (*23*). Order-of-magnitude or greater increases in mechanical strength have been observed when internanotube coupling is enhanced by polymer incorporation into nanotube sheets and yarns (*23*–*26*), and similar strength increases might be achievable by infiltration of suitable polymers into the present MWNT sheets.

Initial results suggest additional promising applications. One is as a stable planar source of polarized UV, visible, and infrared incandescent light (Fig. 3, A and B) for use in sensors, infrared beacons, infrared imaging, and reference signals for device calibration. The degree of polarization of emitted radiation for 2.5% stretched as-drawn sheets increases from 0.71 at 500 nm to 0.74 at 780 nm (Fig. 3B), which is substantially higher than the degree of polarization (0.33 for 500 to 900 nm) previously reported for a 600-μm-long MWNT bundle with an emitting length of ~80 μm (*27*). The wavelength dependence of light intensity for both polarizations fits the functional form expected for black-body radiation, and the degree of polarization does not significantly depend on sheet temperature for the observed temperature range between 1000 and 1600 K. Cost and efficiency benefits result from decreasing or eliminating the need for a polarizer, and the MWNT sheet provides spatially uniform emission over a broad spectral range that is otherwise hard to achieve. The low heat capacity of these very-low-mass incandescent emitters means that they can turn on and off within the observed 0.1 ms or less in vacuum and provide current modulated light output on a shorter time scale.

By simply contacting the as-drawn MWNT sheets to ordinary adhesive tape, we have made optically transparent adhesive appliqués that could be used for electrical heating and for providing microwave absorption (*14*). Because of MWNT sheet porosity, the peel strength is largely maintained when an undensified MWNT sheet is laminated between an adhesive tape and a contacted plastic or metal surface (*14*) (fig. S6). We have used the known microwave absorption capability of MWNTs (*28*, *29*) to demonstrate another possible application: polymer welding through heating of a transparent MWNT sheet that is sandwiched between plastic parts (*14*). Figure 3C shows two 5-mm-thick Plexiglas (polymethyl methacrylate) plates that were welded together using microwave heating of a sandwiched undensified MWNT sheet to provide a strong, uniform, and transparent interface in which nanotube orientation and sheet electrical conductivity are little changed. The combination of high transparency and ultrahigh thermal stability provides advantages

for microwave-based welding not found in the conducting polymers (*30*). This microwave heating process could be used to make polymer composites from stacks of polymer sheets that are separated by nanotube sheets, car windows that are electrically heated, or antennas in car windows that have high transparency.

The work function of these transparent MWNT sheets (~5.2 eV) is slightly higher than that of the ITO typically used as the transparent hole-injecting electrode in organic light-emitting diodes (OLEDs), and these sheets have the additional benefits of being porous and flexible. MWNT sheets made with previous techniques have not been successfully used for optically transmissive, hole-injecting layers in OLEDs: The sheet thickness and surface roughness dwarf the typical 100-nm layer thickness of emissive layers needed for OLEDs (*31*), thereby causing interelectrode shorts; and in thicker devices, the unbalanced hole and electron currents prevent light emission. However, black sheets of solution-spun MWNTs have been used as nontransmissive hole-collecting electrodes in solar cells (*10*), and transparent p-type SWNT sheets have been used as hole-injection electrodes in inorganic LEDs based on gallium nitride (*32*).

We have taken advantage of the nanometer-scale thickness, transparency, flexibility, porosity, and high work function of our densified MWNT sheets to demonstrate polymer-based OLEDs on both flexible plastic and rigid glass substrates (*14*). Hole injection occurs over the high-surface-area interior of the nanoporous nanotube electrode, as opposed to at a planar interface in the previous inorganic LEDs (*32*). The onset voltage for emission is quite low (2.4 V, about the same as for the highest-performance ITO in similar devices), and rather bright electroluminescence was obtained (up to 500 cd/m^2) (fig. S7). The emitted light is slightly polarized, but in an orthogonal direction from that for the above incandescent light source, because the MWNT sheet acts as a polarizer. If a polymeric light-emitting layer were aligned using known methods (*33*) to provide emission in the same polarization direction, absorption due to the MWNT hole injector could be minimized, which is not possible for conventional ITO hole-injecting electrodes.

Although solution- or melt-based processing becomes increasingly difficult as nanofiber length increases, the opposite is true for the present solid-state sheet fabrication process: 300-μm-long nanotubes are easier to convert into sheets than are 70-μm-long nanotubes. Also, ultrasonication used for nanotube dispersion in solution-based processing decreases nanotube length, and this degradative step is absent from the present sheet fabrication process. These are important advantages of the present technology, because long, high-perfection nanotubes are needed for maximizing electrical and thermal conductivities and mechanical properties.

References and Notes

1. A. G. Rinzler *et al.*, *Appl. Phys. A* **67**, 29 (1998).
2. M. Endo *et al.*, *Nature* **433**, 476 (2005).
3. Z. Wu *et al.*, *Science* **305**, 1273 (2004).
4. L. Hu, D. S. Hecht, G. Grüner, *Nano Lett.* **4**, 2513 (2004).
5. J. E. Fischer *et al.*, *J. Appl. Phys.* **93**, 2157 (2003).
6. W. A. De Heer *et al.*, *Science* **268**, 845 (1995).
7. Y. Li, I. A. Kinloch, A. H. Windle, *Science* **304**, 276 (2004).
8. Y. Kim *et al.*, *Jpn. J. Appl. Phys.* **42**, 7629 (2003).
9. T. V. Sreekumar *et al.*, *Chem. Mater.* **15**, 175 (2003).
10. H. Ago, K. Petritsch, M. S. P. Shaffer, A. H. Windle, R. H. Friend, *Adv. Mater.* **11**, 1281 (1999).
11. K. Jiang, Q. Li, S. Fan, *Nature* **419**, 801 (2002).
12. M. Zhang, K. R. Atkinson, R. H. Baughman, *Science* **306**, 1358 (2004).
13. The per-sheet thickness measured by stylus profilometer varied from ~50 to ~150 nm, depending on forest height and draw and densification conditions. Atomic force microscopy provides a sheet thickness of down to 30 to 50 nm, which is close to the maximum width of fibrils in the sheet, which can be far from cylindrical.
14. See supporting data on *Science* Online.
15. P. G. Collins, M. S. Fuhrer, A. Zettl, *Appl. Phys. Lett.* **76**, 894 (2000).
16. H. Ouacha *et al.*, *Appl. Phys. Lett.* **80**, 1055 (2002).
17. L. Roschier, R. Tarkiainen, M. Ahlskog, M. Paalanen, P. Hakonen, *Appl. Phys. Lett.* **78**, 3295 (2001).
18. A 1-mm-thick sheet of silicone rubber (ECOFLEX 0040 from Smooth-On) was stretched to 105% strain, and then a single as-drawn MWNT sheet was laid over it to provide self-generated adhesive contact before strain relaxation. The initial sheet resistance of the obtained unloaded silicone rubber/MWNT sheet composite was 755 ohms per square. However, after an initial increase in resistance by ~6%, the resistance changed less than 3% during the subsequent four strain cycles to 100% strain.
19. R. Pelrine, R. Kornbluh, Q. Pei, J. Joseph, *Science* **287**, 836 (2000).
20. K. Hata *et al.*, *Science* **306**, 1362 (2004).
21. D. E. Edwards *et al.*, *High Perf. Polymers* **16**, 277 (2004).
22. L. M. Ericson *et al.*, *Science* **305**, 1447 (2004).
23. M. E. Kozlov *et al.*, *Adv. Mater.* **17**, 614 (2005).
24. J. N. Coleman *et al.*, *Appl. Phys. Lett.* **82**, 1682 (2003).
25. B. Vigolo, P. Poulin, M. Lucas, P. Launois, P. Bernier, *Appl. Phys. Lett.* **81**, 1210 (2002).
26. A. B. Dalton *et al.*, *Nature* **423**, 703 (2003).
27. P. Li *et al.*, *Appl. Phys. Lett.* **82**, 1763 (2003).
28. P. C. P. Watts, W.-K. Hsu, A. Barnes, B. Chambers, *Adv. Mater.* **15**, 600 (2003).
29. J. Wu, L. Kong, *Appl. Phys. Lett.* **84**, 4956 (2004).
30. A. J. Epstein, A. G. MacDiarmid, *Synth. Metals* **69**, 179 (1995).
31. D. B. Romero, M. Carrard, W. De Heer, L. Zuppiroli, *Adv. Mater.* **8**, 899 (1996).
32. K. Lee, Z. Wu, Z. Chen, F. Ren, S. J. Pearton, A. G. Rinzler, *Nano Lett.* **4**, 911 (2004).
33. K. S. Whitehead, M. Grell, D. D. C. Bradley, M. Jandke, P. Strohriegl, *Appl. Phys. Lett.* **76**, 2946 (2000).

34. Supported by Defense Advanced Research Projects Agency/U.S. Army Research Office grant W911NF-04-1-0174, the Texas Advanced Technology Program grant 009741-0130-2003, the Air Force STTR program on topic AF04-TO20, Air Force grant F49620-03-1-0164, Robert A. Welch Foundation grant AT-0029, and the Strategic Partnership for Research in Nanotechnology consortium in Texas. The authors thank J. P. Ferraris and M. Zhou for the synthesis of the emissive polymer used for the OLEDs, A. Kuznetsov for assistance with OLED preparation, and V. H. Ebron for assistance with the microwave welding.

Supporting Online Material

www.sciencemag.org/cgi/content/full/309/5738/1215/DC1
Materials and Methods
Figs. S1 to S7
References
Movies S1 and S2

25 May 2005; accepted 13 July 2005
10.1126/science.1115311

Understanding the Infrared Spectrum of Bare CH_5^+

Oskar Asvany,[1]* Padma Kumar P,[2]* Britta Redlich,[3] Ilka Hegemann,[2] Stephan Schlemmer,[1,4] Dominik Marx[2]†

Protonated methane, CH_5^+, continues to elude definitive structural assignment, as large-amplitude vibrations and hydrogen scrambling challenge both theory and experiment. Here, the infrared spectrum of bare CH_5^+ is presented, as detected by reaction with carbon dioxide gas after resonant excitation by the free electron laser at the FELIX facility in the Netherlands. Comparison of the experimental spectrum at ~110 kelvin to finite-temperature infrared spectra, calculated by ab initio molecular dynamics, supports fluxionality of bare CH_5^+ under experimental conditions and provides a dynamical mechanism for exchange of hydrogens between CH_3 tripod positions and the three-center bonded H_2 moiety, which eventually leads to full hydrogen scrambling. The possibility of artificially freezing out scrambling and internal rotation in the simulations allowed assignment of the infrared spectrum despite this pronounced fluxionality.

Protonated methane, CH_5^+, is of great interest in vibrational spectroscopy (*1–4*) as the prototype of hypercoordinated carbon and three-center two-electron bonding (*5*, *6*). The equilibrium structure—that is, the global minimum of its potential energy surface (PES)—can be viewed as a CH_3 tripod with a H_2 moiety attached to the carbon in an eclipsed C_s configuration, e-C_s, via a three-center bond (*7*). However, rapid hydrogen scrambling has called into question the notion of assigning it such a traditional molecular structure (*8–11*), despite the stability of CH_5^+ once it is formed (*12*). This fluxionality has been traced back